Frontiers in Computing and Intelligent Systems
ISSN: 2832-6024 | Vol. 18, No. 2, 2026

A Hyperbola-Prior-Guided Initialization Strategy for Ground-Penetrating Radar Waveform Inversion

Yukui Zhang, Ying Liu *, Yuxin Ji, Zewen Zi

School of Electronic Engineering, Tianjin University of Technology and Education, Tianjin, 300322 China
* **Corresponding author**: Ying Liu (Email: liuying@tute.edu.cn)

Abstract: Ground-penetrating radar (GPR) waveform inversion is sensitive to the initial model. This study proposes a hyperbola-prior-guided initialization strategy for two-dimensional GPR permittivity inversion. B-scan preprocessing, robust hyperbola fitting, and bootstrap resampling are used to estimate target geometry and positional uncertainty. The fitted prior, an engineering radius constraint, and uncertainty estimates define an adaptive region; envelope- and amplitude-based coarse scanning selects an initial anomaly permittivity without using the true target value. Four initial models—a homogeneous background (M1), a perturbed model (M2), a hard-boundary prior model (M3), and a sigmoid soft-boundary model (M4)—are compared under identical inversion settings. Simulations of a single PVC pipe in homogeneous soil show that the prior-informed models offer complementary benefits relative to conventional initializations. The main trends remain stable across tested noise levels: M3 provides better regional and boundary reconstruction when the geometric prior is accurate, whereas M4 generally yields smaller target-center errors and lower ROI-RMSE degradation under the tested geometric perturbations.

Keywords: Ground-penetrating Radar; Hyperbola Prior; Initialization Strategy; Permittivity Inversion.

1. Introduction

Ground-penetrating radar (GPR) provides spatially continuous responses for detecting and characterizing shallow subsurface targets. Numerical tools such as gprMax enable controlled studies of GPR forward modeling and inversion [1]. However, quantitative permittivity reconstruction through waveform inversion remains challenging because the optimization is nonlinear and sensitive to the initial model; unsuitable initialization may lead to inaccurate updates or undesired solutions.

For cylindrical or pipe-like targets, B-scans commonly contain hyperbolic events whose geometry encodes target position, depth, and size. Previous studies have developed hyperbola fitting, automated feature detection, and parameter-estimation methods, including approaches for incomplete hyperbolas and noisy responses [2–4]. In parallel, GPR waveform inversion has advanced through multiscale strategies, total-variation regularization, and envelope-based objectives [5–8]. These methods improve geometric interpretation or inversion performance, but geometric information extracted from hyperbolas is not always converted into spatial initial permittivity models. In particular, how uncertain geometric estimates should be represented, and whether a hard boundary or a continuous soft boundary is more suitable for initialization, remains insufficiently understood.

This study proposes a hyperbola-prior-guided initialization strategy for two-dimensional GPR waveform inversion. The fitted geometry, an engineering radius prior, and estimated positional uncertainty are used to define an adaptive region, while envelope- and amplitude-based coarse scanning selects the initial anomaly permittivity without using the true target value. Four models are compared under identical inversion settings: a homogeneous background (M1), a perturbed model (M2), a hyperbola-informed hard-boundary model (M3), and a sigmoid soft-boundary model (M4). Their performance is evaluated under different noise levels and geometric perturbations, focusing on regional reconstruction, target localization, and robustness. The study is limited to a two-dimensional homogeneous background containing a single PVC pipe.

2. Methodology

2.1. Hyperbola Prior Extraction

The B-scan data were processed by background subtraction, detrending, band-pass filtering, and Hilbert-envelope calculation. The main hyperbolic event was extracted within the 7-16 ns time window and fitted using the bistatic travel-time model in Eq. (1), assuming a known background permittivity ε_b.

$$t(x)=t_f+\frac{\sqrt{z_{top}^2+\left(x-x_c-\frac{o}{2}\right)^2}+\sqrt{z_{top}^2+\left(x-x_c+\frac{o}{2}\right)^2}}{v} \quad (1)$$

where x_c and z_{top} are the target horizontal position and top depth, o is the transmitter – receiver offset, t_f = 1.571 ns is the fixed wavelet delay, and v is the background propagation velocity. RANSAC (300 iterations; 0.30-ns inlier threshold) was followed by Huber-loss refinement [9]. Bootstrap resampling (120 repetitions) estimated positional uncertainty [10]. The fitted values were x_c = 0.59998 m, z_{top} = 0.64015 m, and z_{c0} = 0.70015 m, with σ_x = 0.00659 m and σ_z = 0.00113 m.

2.2. Prior-Guided Initial Model Construction

The target-center depth was estimated as $z_{c0}=z_{top}+r_0$ where r_0 is the engineering radius prior. The region of interest (ROI) was defined using the hyperbola-fitted target geometry, the engineering radius prior, and the estimated positional uncertainties. The resulting ROI was used consistently for initial-model construction and ROI-based performance evaluation, ensuring that the four models were compared over the same spatial region. The initial anomaly

permittivity was selected by coarse scanning over ε_a = 2.0-5.0 in increments of 0.5, using $J_{coarse} = 0.75J_{env} + 0.25J_{amp}$. The selected value was ε_a = 4.0, without using the true target permittivity.

Four initial models were compared. M1 was a homogeneous background model. M2 was a controlled perturbed-anomaly model in which the anomaly geometry was perturbed relative to the reference configuration. M3 used a circular hard boundary defined by the hyperbola-fitted geometry, whereas M4 employed a sigmoid soft boundary to represent geometric uncertainty. The four models were evaluated using the same inversion settings to isolate the effects of their initial-model representations.

$$M(x,z)=\left[1+\exp\left(\frac{d(x,z)}{\tau}\right)\right]^{-1}. \quad (2)$$

where $d(x,z)$ is the signed distance to the estimated target boundary and τ=0.010 m controls the transition width. Inside the estimated target d<0 and outside it d>0. The soft-boundary model is $\varepsilon_{init(x,z)} = \varepsilon_b + M(x,z)(\varepsilon_{ainit} - \varepsilon_b)$, where ε_a,init is the scanned anomaly permittivity; outside the ROI, ε_{init} remains ε_b. For M3, M is a binary mask with an abrupt boundary. The four initial permittivity models are illustrated in Fig. 1.

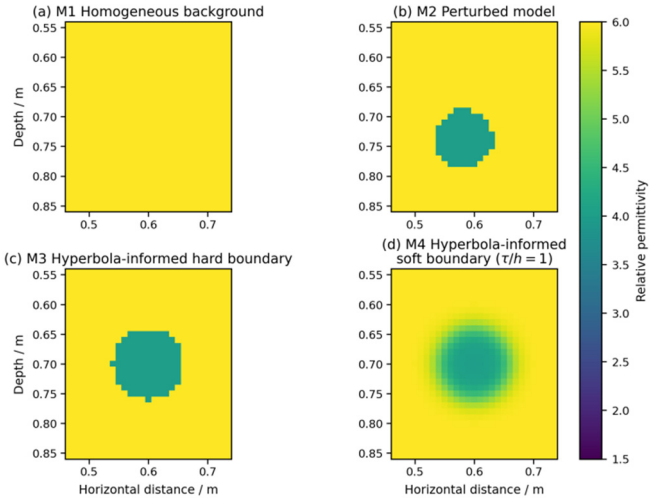


Figure 1. Initial permittivity models used for waveform inversion.

2.3. Waveform Inversion and Evaluation

All four initial models were inverted using the same forward model, objective function, regularization, optimizer, parameter bounds, and iteration budget. The objective minimized normalized waveform misfit with total-variation regularization, as defined in Eq. (3).

$$J = \frac{1}{2}\frac{\|W(d_{cal} - d_{obs})\|_F^2}{\|Wd_{obs}\|_F^2} + \lambda TV_\beta(\varepsilon_r), \quad (3)$$

where d_{cal} and d_{obs} are the calculated and observed scattered fields, respectively. The parameter λ controls the strength of total-variation regularization, while β denotes the smoothing parameter used in the TV regularization term. Projected steepest descent with Armijo line search was employed, with conductivity fixed, relative permittivity constrained to [1.5, 8.0], λ=0.001, β=0.010, and a maximum of 10 iterations. Reconstruction performance was evaluated using ROI RMSE, Dice coefficient, and target-center error.

3. Numerical Experiments

3.1. Numerical Model

The experiments were restricted to a controlled two-dimensional single-target configuration so that the effect of geometric prior information on initialization could be evaluated independently of complex geological heterogeneity and multiple-target interference. A two-dimensional GPR model consisting of homogeneous soil and a single cylindrical PVC pipe was simulated using gprMax. The background and target relative permittivities were ε_b = 6.0 and ε_{true} = 3.0, respectively. The pipe radius was 0.060 m, and its center was located at (x, z) = (0.60, 0.70) m. The forward-model and inversion grid spacings were 0.005 and 0.010 m, respectively. A 0.90 GHz Ricker source was used with 43 traces at 0.020 m spacing, a 0.040 m transmitter–receiver offset, and an 18 ns time window. All four initial models were evaluated using identical observed data and inversion settings.

3.2. Experimental Design

Noise robustness was assessed at SNRs of 20, 15, and 10 dB using 10 independent noise realizations per level. Geometric uncertainty was evaluated under 12 non-zero, one-factor-at-a-time conditions: horizontal-position and depth offsets of ± 0.02 and ± 0.05 m, and radius offsets of ± 0.010 and ± 0.020 m. The radius offsets correspond to relative errors of approximately ± 16.7% and ± 33.3% for a reference radius of 0.060 m. M3 and M4 were evaluated under each condition, while zero-perturbation baselines were reused and excluded from the count. A separate validation at 15 dB used five noise realizations for each of three perturbations: Δx = + 0.05 m, Δz = + 0.05 m, and Δr = + 0.020 m.

4. Results and Conclusion

4.1. Comparison of Initial Models

Under noise-free conditions, the four initial models produced distinct inversion results (Fig. 2). Compared with M1 and M2, the hyperbola-prior models M3 and M4 provided more informative spatial constraints. M1 remained close to the background model and failed to recover the target region, whereas M2 reconstructed only part of the anomaly and showed a mismatch with the true target boundary. These results indicate that a reduction in waveform misfit alone does not guarantee accurate spatial reconstruction.

M3 recovered a compact target region with a boundary closely matching the reference circle. Its convergence curve also reached the lowest final normalized data misfit among the four models. M4 produced a smoother and more diffuse anomaly, consistent with its sigmoid boundary representation. Its final data misfit was lower than those of M1 and M2, but its reconstructed boundary was less sharply localized than that of M3. This contrast reflects the different roles of the two priors: the hard boundary preserves geometric localization when the estimated geometry is accurate, whereas the soft boundary distributes the contrast across a transition zone and may better accommodate small geometric errors. Therefore, data misfit and spatial reconstruction metrics should be interpreted together when comparing initialization strategies.

4.2. Robustness to Noise

Across SNRs of 20, 15, and 10 dB, the performance trends of M3 and M4 remained relatively stable (Table 1). M3 consistently achieved lower ROI RMSE (0.5720-0.5723) and

higher Dice coefficients (0.9843-0.9861), indicating better regional reconstruction and boundary overlap. In contrast, M4 yielded smaller target-center errors of 1.39-1.42 mm, compared with 2.42-2.48 mm for M3. These results demonstrate a trade-off between regional reconstruction and target localization rather than universal superiority of either boundary representation.

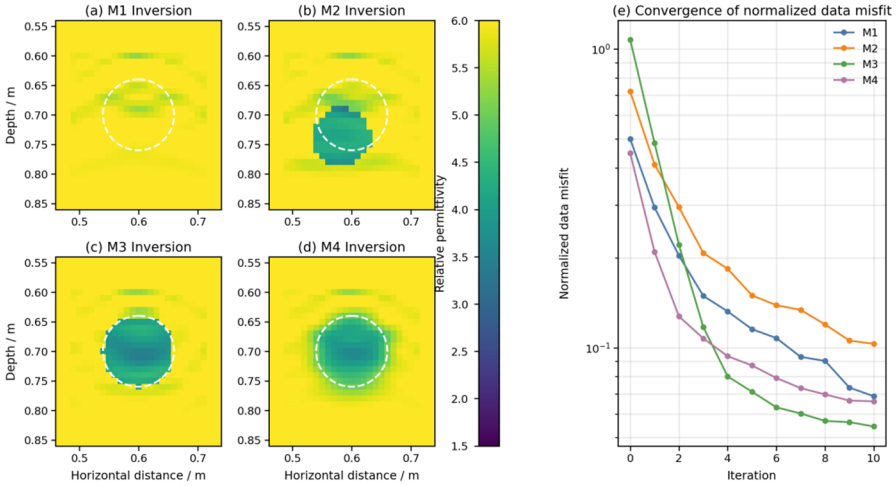


Figure 2. Noise-free inversion results and convergence of normalized data misfit for M1–M4. White dashed circles indicate the true target boundary.

Table 1. Performance of M3 and M4 under different noise levels

Nominal SNR (dB)	Model	ROI RMSE	Center error (mm)	Dice
20	M3	0.5720 ± 0.0001	2.45 ± 0.12	0.9861 ± 0.0014
20	M4	0.7314 ± 0.0001	1.39 ± 0.05	0.7892 ± 0.0053
15	M3	0.5721 ± 0.0002	2.42 ± 0.12	0.9847 ± 0.0032
15	M4	0.7314 ± 0.0001	1.40 ± 0.06	0.7879 ± 0.0052
10	M3	0.5723 ± 0.0002	2.48 ± 0.13	0.9843 ± 0.0039
10	M4	0.7315 ± 0.0002	1.42 ± 0.11	0.7930 ± 0.0093

Note: Values are mean ± SD over 10 independent noise realizations; ROI RMSE is computed within the fixed evaluation region.

4.3. Effect of Geometric Uncertainty

Across the 12 non-zero, one-factor-at-a-time geometric perturbation conditions, M4 achieved a lower ROI RMSE in 11 conditions and a lower target-center error in 10. However, its Dice coefficient was higher in only one condition, indicating that improved localization and regional reconstruction do not necessarily coincide with better boundary overlap. The relative ROI-RMSE degradation was also lower for M4 across all 12 conditions. These results suggest that the sigmoid soft boundary improves tolerance to geometric uncertainty, particularly for target localization, whereas the hard-boundary model M3 remains advantageous for regional overlap when the geometric prior is sufficiently accurate. Neither model was uniformly superior across all evaluation metrics.

Acknowledgments

This work was supported by the National Natural Science Foundation of China (Grant No. 62241109), and Scientific Research Fund of Tianjin Education Commission (Grant No. 2021KJ005).

References

[1] Warren, C., Giannopoulos, A., & Giannakis, I. (2016). gprMax: Open source software to simulate electromagnetic wave propagation for ground penetrating radar. Computer Physics Communications, 209, 163–170. https://doi.org/10.1016/j.cpc.2016.08.018.

[2] He, W., & Lai, W. W. L. (2024). Unified optimization-based analysis of GPR hyperbolic fitting models. Tunnelling and Underground Space Technology, 146, 105633. https://doi.org/10.1016/j.tust.2024.105633.

[3] Zhu, C., & Ye, H. (2023). A modular method for GPR hyperbolic feature detection and quantitative parameter inversion of underground pipelines. Remote Sensing, 15(8), 2114. https://doi.org/10.3390/rs15082114.

[4] He, W., & Lai, W. W. L. (2026). Modelling incomplete GPR hyperbolas. NDT & E International, 162, 103746. https://doi.org/10.1016/j.ndteint.2026.103746.

[5] Feng, D., Cao, C., & Wang, X. (2019). Multiscale full-waveform dual-parameter inversion based on total variation regularization to on-ground GPR data. IEEE Transactions on Geoscience and Remote Sensing, 57(11), 9450–9465. https://doi.org/10.1109/TGRS.2019.2926042.

[6] Meles, G., Greenhalgh, S., van der Kruk, J., et al. (2011). Taming the non-linearity problem in GPR full-waveform inversion for high contrast media. Journal of Applied Geophysics, 73(2), 174–186. https://doi.org/10.1016/j.jappgeo.2011.01.004.

[7] Jazayeri, S., Klotzsche, A., & Kruse, S. (2018). Improving estimates of buried pipe diameter and infilling material from ground-penetrating radar profiles with full-waveform inversion. Geophysics, 83(4), H27–H41. https://doi.org/10.1190/geo2017-0526.1.

[8] Liu, X., Liu, S., Luo, C., et al. (2022). Source-independent waveform inversion method for ground-penetrating radar based on envelope objective function. Remote Sensing, 14(19), 4878. https://doi.org/10.3390/rs14194878.

[9] Fischler, M. A., & Bolles, R. C. (1981). Random sample consensus: A paradigm for model fitting with applications to image analysis and automated cartography. Communications of the ACM, 24(6), 381–395. https://doi.org/10.1145/358669.358692.

[10] Efron, B. (1979). Bootstrap methods: Another look at the jackknife. The Annals of Statistics, 7(1), 1–26. https://doi.org/10.1214/aos/1176344552.